

The Soft X-Ray Emission Surrounding Starburst-driven High-velocity Molecular Clouds in the Galactic Center

Pei-Xin Zhu, Miao Li, and Meng-Fei Zhang

School of Physics, Zhejiang University, Hangzhou 210023, China; peisinchoo@zju.edu.cn, miaoli@zju.edu.cn, murphychang@zju.edu.cn
Received 2024 December 13; revised 2025 June 13; accepted 2025 August 5; published 2025 October 17

Abstract

This study numerically investigates the formation of high-velocity molecular clouds (HVMCs) in the Galactic Center (GC) based on the X-ray emission analysis. We employ three-dimensional magnetohydrodynamic simulations to explore the propagation and acceleration of HVMCs with starburst-driven winds, considering vertical, horizontal, and no magnetic field scenarios. Our results reveal that the envelope gas (with a typical $T \sim 10^8$ K and density $\sim 10^{-2}$ cm⁻³) of molecular clouds (MCs) as a result of the shock interaction is responsible for X-ray emission. Additionally, some clear boundary exists between the interstellar medium (ISM), envelope gas and MCs, and the envelope gas protects the MCs in the heated environment of the shock wave. In theory, it is challenging to distinguish between the envelope gas, MCs and ISM in terms of X-ray emission. Our simulations suggest that the envelope gas has a significant impact on the survival and emission characteristics of MCs, providing insights into the complex interactions from the supernova feedback mechanisms in the GC.

Key words: methods: data analysis – Galaxy: center – galaxies: starburst – radiation mechanisms: thermal – ISM: clouds – ISM: lines and bands

1. Introduction

In recent decades, extensive research has been conducted on galaxy formation and evolution, particularly regarding the role of nuclear winds in galaxy feedback, which are considered crucial for galaxy evolution (e.g., Fabian 2012; Heckman & Best 2014; Heckman & Thompson 2017; Naab & Ostriker 2017; Zhang 2018, and references therein). Current theory and simulation results predict that the galactic stellar mass function exhibits a Schechter-like mass function (Naab & Ostriker 2017), but there are differences in the galactic stellar mass function between observations and simulations. It is currently hypothesized that these discrepancies arise due to the influence of galaxy feedback, which may suppress the formation of lowmass galaxies and hinder the detection of high-mass galaxies. To investigate these phenomena further, we focus on studying intense physical processes, such as nuclear winds, which are thought to play a significant role in the galactic stellar mass function. Current observations of the Milky Way's center do not reveal strong nuclear winds (Baganoff et al. 2003; Haywood et al. 2016). Some speculated that nuclear winds may alternate between active and quiescent phases, implying that vigorous activity should leave relics (Baganoff et al. 2003; Haywood et al. 2016). Over the past few decades, potential relics have been observed in radio, X-ray, and γ -ray wavelengths, including the Galactic Center Lobe (GCL; Sofue & Handa 1984), microwave halo (Finkbeiner 2004; Planck Collaboration et al. 2013), X-ray chimneys (Ponti et al. 2019), polarized lobes (Carretti et al. 2013), radio bubbles

(Heywood et al. 2019), Fermi bubbles (Su et al. 2010), and eROSITA bubbles (Predehl et al. 2020). These structures arise from a series of intense physical processes (Bland-Hawthorn et al. 2019), spanning scales from 100 pc to 10 kpc. Due to the difficulty in distinguishing these relics, the focus of the study is shifted to high-velocity clouds (HVCs), which are thought to form under more stringent conditions. The goal is to gain insights into galaxy feedback mechanisms by investigating the properties and dynamics of these HVCs. By studying HVCs, we aim to establish a better understanding of how galaxy feedback influences the interstellar medium (ISM) and galaxy formation processes.

HVCs have been observed at the Galactic Center (GC), distributed above and below the Galactic plane (Collins et al. 2004, 2005; Di Teodoro et al. 2018; Ashley et al. 2020; Lockman et al. 2020). Research by Di Teodoro et al. (2020) indicates the presence of high-velocity molecular clouds (HVMCs) approximately 0.9 kpc above and 0.6 kpc below the Galactic plane, moving at local standard of rest (LSR) ~ 180 and $150 \,\mathrm{km \, s^{-1}}$ along the z-axis, respectively. These HVMCs may be part of the aforementioned relics, which are influenced by nuclear winds. Three-dimensional (3D) magnetohydrodynamic (MHD) simulations by Zhang & Li (2024) have illustrated the propagation of HVMCs on kpc scales. However, there remains controversy regarding the dominant physical processes at the GC. The prevailing view suggests that the formation of Fermi bubbles is primarily attributed to two processes: the activity of supermassive black holes (SMBHs)

(e.g., Guo & Mathews 2012; Zubovas & Nayakshin 2012; Zhang & Guo 2020) or starbursts (e.g., Fujita et al. 2013; Lacki 2014; Sarkar et al. 2015; Zhang et al. 2021), each displaying distinct observational characteristics. The acceleration of molecular clouds (MCs) induced by SMBH activity does not involve thermal X-ray emissions with high metallicity.

In galaxies with a high star formation rate (SFR), a large number of stars are formed, and among them, massive stars quickly evolve to the end stages of their lives, culminating in supernova (SN) explosions. In such environments, the starburst-driven winds are primarily driven by the energy released from these SNe. As a result, the winds generated by starbursts in these galaxies are enriched with a significant proportion of heavy metals, which are ejected during the SN explosions. This enrichment plays a key role in the chemical evolution of the ISM and the broader galactic environment, thereby supporting this theory through observations of specific elemental line spectra and the X-ray spectra (Fujita et al. 2013; Lacki 2014; Sarkar et al. 2015; Zhang et al. 2021). The origin of HVMCs remains debated, and it is difficult to accelerate them to high velocities without destroying the MCs in simulations to form HVMCs (Schneider & Robertson 2017; Cashman et al. 2021). Given that the remnants in the GC are thought to result from a series of intense physical processes, the mechanisms that form Fermi bubbles likely also contribute to the acceleration of MCs.

In the study by Zhang & Li (2024), the SN explosions were simulated to drive the MCs to velocities of approximately 200 km s⁻¹, supporting the theory that MCs maintain a highdensity state during intense physical processes. In the simulation by Zhang & Li (2024), magnetic fields were included, allowing MCs to form and survive as HVMCs under the influence of shock waves. The shock compression increases the magnetic pressure, which contributes to the acceleration of the MCs. A reverse shock forms at the interface between the shock front and the MCs, gradually reducing the acceleration of the clouds. When the MCs reach higher latitude regions, their velocity can reach up to $\sim 400 \,\mathrm{km \, s^{-1}}$. In lower latitude regions, the clouds mix more extensively with the SN ejecta, leading to an increase in the metallicity of the MCs. The simulation studies have also shown that HVMCs can be accelerated to high latitudes by starbursts at the GC, providing valuable insights into their survival mechanisms (Zhang & Li 2024).

However, this study did not elaborate on how MCs are accelerated to velocities on the order of $\sim \! 100 \, \mathrm{km \, s^{-1}}$. To explore the specific physical processes influencing MC acceleration, this paper will further analyze the data from Zhang & Li (2024). We will compute the soft X-ray continuum spectrum to investigate the acceleration process under the influence of starbursts. Additionally, we will utilize the $AtomDB^1$ database to calculate the X-ray spectral lines of

O VII, O VIII and Fe L-shell, comparing these with observational data (Pan et al. 2024) to validate the impact of SNe on MCs. Through the calculation of the soft X-ray continuum spectrum and the line spectrum of O VII, O VIII and Fe L-shell, this study elucidates the soft X-ray conditions in HVMCs and analyzes the acceleration of MCs driven by starburst-induced winds. We will also slice through the density, temperature, magnetic field, velocity field, and X-ray flux in a direction perpendicular to the Galactic plane, revealing that MCs are heated by shock waves and reverse shocks, which leads to X-ray emissions from the MCs.

This paper will describe the simulation setup in Section 2 and show the results in Section 3. The X-ray emission of HVMCs will be discussed in Section 4. Section 5 is a summary.

2. Simulation

In this work, we utilize the 3D MHD code *PLUTO*² (e.g., Mignone et al. 2007, 2012). This grid-based MHD code employs a second-order Runge–Kutta time integrator combined with the Harten-Lax-van Leer Riemann solver to effectively handle intermediate contact discontinuities, allowing for accurate simulations of SN shock waves and their interactions with MCs.

In this paper, we will use two terms to describe gas under certain conditions: 1. high density and low temperature; 2. low density and high temperature. The definitions for these descriptors are as follows:

- 1. High Density and Low Temperature: Gas temperature $T \lesssim 10^4 \,\mathrm{K}$ and density $n \gtrsim 10 \,\mathrm{H\,cm^{-3}}$, where ions and neutral gas are mixed; this gas primarily exists in MCs.
- 2. Low Density and High Temperature: Gas temperature $T \gtrsim 10^8 \,\mathrm{K}$ and density $n \lesssim 10^{-2} \,\mathrm{H\,cm}^{-3}$, where the gas is generally fully ionized; this condition is mostly found in envelope gas and in the ISM affected by shocks.

2.1. Basic Configuration

The simulation is set in a 3D MHD Cartesian frame. The grid has a size of $200 \times 200 \times 2000$, representing a physical volume of $100 \times 100 \times 1000 \,\mathrm{pc^3}$ with a linear resolution of $0.5 \,\mathrm{pc}$ per pixel. The z-axis is perpendicular to the Galactic disk (the positive direction is north), the y-axis runs along decreasing Galactic longitude, and the x-axis is parallel to the line-of-sight (with the observer located on the negative side). An outflow boundary condition is applied in all directions, allowing some of the clouds' material to flow outside the simulation box.

To characterize the gravitational potential in the simulation, we assume that the potential is determined by an SMBH, a

¹ http://www.atomdb.org

http://plutocode.ph.unito.it/

nuclear star cluster (NSC), and a nuclear disk (ND), with the potential field being static. In the simulation, the SMBH is represented as a point mass of $4 \times 10^6 M_{\odot}$. We employ the spherically symmetric distribution model proposed by Chatzopoulos et al. (2015) (see Equation (5) of that paper) to describe the NSC and ND (see Appendix A). For the effects of radiative cooling in the simulation, we use a piecewise cooling function with a minimum cooling temperature set to 100 K (see Appendix B). The chemical composition of the ISM and the initial MCs is assumed to be solar, with hydrogen abundance $X_{\odot} = 0.711$, helium abundance $Y_{\odot} = 0.2741$, and metallicity $Z_{\odot} = 0.0149$. The multiphase gas at the center of the Milky Way includes components at different temperatures, such as high-temperature ionized gas ($\sim 10^6$ K; Kataoka et al. 2013; Ponti et al. 2019), warm ionized gas (between 10⁴ and 10⁵ K; Fox et al. 2015; Bordoloi et al. 2017), and cold atomic gas (between 10³ and 10⁴ K; McClure-Griffiths et al. 2013; Di Teodoro et al. 2018).

2.2. Supernova Explosion and Molecular Clouds

The initial conditions of the simulation are set based on observational data and analytical models. Observationally, the density range of HVMCs typically falls between 10 and 300 cm⁻³, with outflow velocities ranging from 200 to 300 km s⁻¹ (Di Teodoro et al. 2020). However, considering the gas mass loss during the propagation of HVMCs, we set the initial density of the MCs higher than the observed range. Since MCs can be destroyed by SN-driven winds, we need to consider the SN explosion frequency and the initial latitude of the MCs to reach the velocities observed by Ponti et al. (2019). Here, we introduce the cloud disruption timescale

$$t_{\rm cc} = \frac{r_{\rm mc}}{v_{\rm sn}} \sqrt{\frac{\rho_{\rm mc}}{\rho_{\rm sn}}}.$$
 (1)

The cloud disruption timescale quantifies the time for MCs to be destroyed by the winds (Klein et al. 1994), where $r_{\rm mc}$ is the initial radius of the MC, $\rho_{\rm mc}$ is the cloud density, $v_{\rm sn}$ is the wind speed generated by the SN, and $\rho_{\rm sn}$ is the wind density. When the evolution time exceeds $t_{\rm cc}$, the cloud is gradually destroyed and is completely disrupted after approximately $2t_{\rm cc}$. However, this timescale does not consider the effects of magnetic fields and cooling mechanisms, which may significantly influence the evolution of the clouds.

We set the SN to explode within a cylindrical region with a radius of 35 pc and a latitude of 10 pc, with an SN birth rate of 10 kyr^{-1} (Di Teodoro et al. 2018). The center of the cylindrical region is positioned 100 pc west of Sgr A*. We assumed an SFR of $1 M_{\odot} \text{ yr}^{-1}$, using the initial mass function (IMF) from Kroupa (2001), and we assumed that core-collapse SNe originate from stars with a minimum mass of $8 M_{\odot}$. Type Ia SNe are neglected, as their estimated birth rate within the ND/NSC is $\lesssim 0.05 \text{ kyr}^{-1}$ (Mannucci et al. 2005). SNe are set to

explode randomly within the cylindrical region, using the same random seed across all simulations.

The density of the MCs in the simulation follows an inverse square law distribution, expressed as $n_{\rm mc} = n_0/r^2$, where n_0 is the central density and $r_{\rm mc}$ is the radius. In simulations with a vertical magnetic field, we set $n_0 = 1500\,{\rm H\,cm^{-3}}$, with an initial maximum radius of 10 pc for the MCs, positioned 50 pc above the galactic plane. Based on these parameters ($r_{\rm mc} = 10\,{\rm pc}$, $v_{\rm sn} = 1000\,{\rm km\,s^{-1}}$, $n_{\rm mc} = 15 \sim 50\,{\rm H\,cm^{-3}}$, and $n_{\rm sn} = 0.01\,{\rm H\,cm^{-3}}$), we estimate $t_{\rm cc} = 1 \sim 2\,{\rm Myr}$. Thus, in classical analyses, the cloud would completely disperse after 4 Myr. However, in our preliminary tests, we found that when considering vertical magnetic fields and cooling effects, the cloud can survive for over 7 Myr. In this scenario, after approximately 7 Myr, the cloud will extend beyond the simulation box. Therefore, the simulation results will be presented up to about 7 Myr.

The simulation tracks the mixing of injected ejecta with MCs, which alters the metallicity of the clouds. This is achieved through two tracer parameters, Q_1 and Q_2 , calculated at each pixel and following the conservation law

$$\frac{\partial(\rho Q_i)}{\partial t} + \nabla \cdot (\rho Q_i v) = 0. \tag{2}$$

 Q_1 is 1 for pure SN ejecta and 0 for unpolluted MCs and ISM, while Q_2 is 1 for pure MCs and 0 for unpolluted SN ejecta and ISM. Intermediate values indicate mixed gas. These parameters enable tracking of the mixing process and analysis of the metal distribution in the system over time.

2.3. The ISM and the Magnetic Field

We assume that the density and temperature of the ISM during initialization are uniformly distributed throughout the simulation box, set to 0.01 H cm⁻³ and 10⁶ K, respectively. It is important to note that the simulation employs a nonequilibrium initial environment, as the static equilibrium is not crucial for our study. At its birth, a galaxy should be in approximate hydrostatic equilibrium (with higher thermal pressure in low-latitude regions), but this equilibrium will be disrupted at early age by the shocks produced by SN explosions or active galactic nucleus (AGN) winds. Our Milky Way has already passed its childhood, thus the hydrostatic balance has been broken. Therefore, it is not necessary to set an initial condition consistent with a hydrostatic equilibrium. In our simulation, the simulation box will be quickly dominated by the shock winds, which is already reliable for understanding the survival of clouds.

The magnetic field distribution in the GC remains unclear, especially within a few tens of pc from the GC (Ferrière 2009). The different components of the surrounding medium influence both the strength and direction of the magnetic field. While there is a large-scale overall model for the entire Milky

Way (e.g., Beck et al. 2013; Cerri et al. 2017), where the magnetic field is parallel to the galactic plane at low latitudes and gradually becomes vertical at higher latitudes, this only serves as an approximation within the GC. Therefore, in this study, we test scenarios with vertical, horizontal and no magnetic fields separately.

The magnetic field strength is approximately $\sim 1 \, \text{mG}$ at distances of a few tens of pc from the GC (Ferrière 2009) and decreases to a few μG at 1 kpc above the galactic plane (Cerri et al. 2017). To simplify the simulation, we adopt a uniform magnetic field strength of $10 \, \mu \text{G}$ throughout the simulation box.

In addition, we perform three runs with different magnetic configurations, vertical and horizontal to the Galactic plane, and without a magnetic field, which are respectively called f100n15000v, f100n15000h and f100n15000n. Here f100n15000v is taken as the fiducial run.

2.4. X-Ray Band and Cooling Curve

In this study, the mechanisms primarily responsible for X-ray emission are bremsstrahlung (continuous spectrum radiation) and line emission (spontaneous radiation caused by collisional ionization). The end stages of massive stars' evolution in starburst regions lead to SN explosions, which drive shocks that generate high-temperature plasma. The X-rays emitted from high-energy free electrons colliding within this plasma are referred to as bremsstrahlung radiation, typically appearing as a continuous spectrum. We calculate the flux for a temperature range $10^4 \,\mathrm{K} < T < 10^9 \,\mathrm{K}$. Within this range, ionized particles can provide a sufficient number of free electrons for collisions. These collisions excite atoms or ions, causing them to emit X-rays, which typically appear as line spectra (Draine 2010).

In low-density conditions, each excitation from a collision results in radiative losses, leading to the cooling rate per unit volume expressed as

$$C = n^2 \Lambda(T), \tag{3}$$

where $\Lambda(T)$ is the radiative cooling function, a function of temperature T.

When plotting the X-ray flux, it is essential to use the cooling function to compute the numerical values of the X-ray flux. In this paper, data from the *AtomDB* database are utilized for the cooling function calculations. Equation (3) represents the cooling function, using an energy band of 0.5–2 keV, which includes elements: H, He, C, N, O, Ne, Mg, Al, Si, S, Ar, Ca, Fe, and Ni.

Notably, when considering X-ray flux, the flux is evidently proportional to the square of the density, as indicated in Equation (3). Within the range of $10^5 < T < 10^6 \,\mathrm{K}$, $\Lambda(T)$ increases sharply with temperature. Therefore, within this temperature range, the influence of temperature on the X-ray

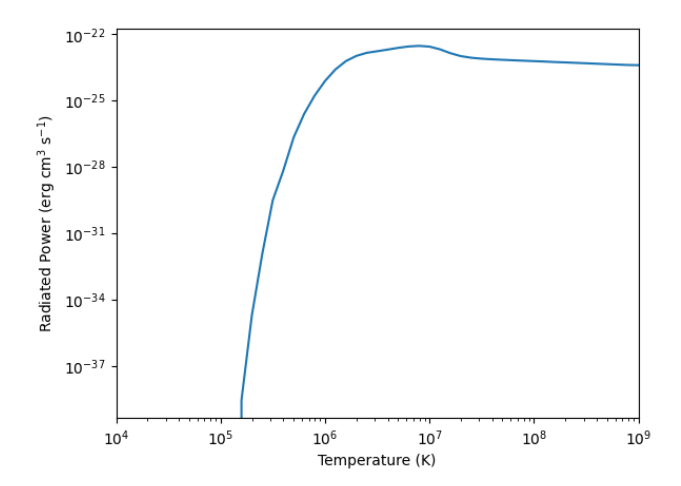


Figure 1. Cooling curve used in calculating radiative cooling.

flux is larger than that of density, so lower temperatures result in lower flux. When temperatures are above $10^6 \, \mathrm{K}$, the relationship between flux and temperature becomes more gradual, and the influence of density on the X-ray flux exceeds that of temperature, meaning that lower densities result in lower flux.

We employed the *PyAtomDB*³ library to access the *AtomDB* database and to plot the cooling rate curve shown in Figure 1. By selecting specific elements, energy bands, and temperature ranges, one can compute X-ray flux data for specific spectral lines (Foster et al. 2016). After obtaining the data from *AtomDB* through calculations with *PyAtomDB*, we fitted the cooling rate curve data and used simulated data for density *n* and temperature *T* from Zhang & Li (2024) to calculate the X-ray flux.

3. Result

In this study, the objective is to investigate the thermal X-ray emission spectrum generated under the influence of starbursts. We do not consider X-ray data with temperatures below 10^4 K. We classify clouds with a density greater than $10 \, \mathrm{H \, cm^{-3}}$ as MCs and those with densities in the range of $1{\text -}10 \, \mathrm{H \, cm^{-3}}$ as atomic clouds. The gas can be divided into two regions based on the tracers Q_1 and Q_2 described in Section 2.2, as follows: (1) Region A: The region containing gas affected by SNe, as indicated by the tracer Q_1 ; (2) Region B: The region containing MC components, as indicated by the tracer Q_2 .

Section 3.1 describes the evolution of X-ray flux with a vertical magnetic field. Section 3.2 discusses the evolution with horizontal and no magnetic field.

https://atomdb.readthedocs.io/en/master/

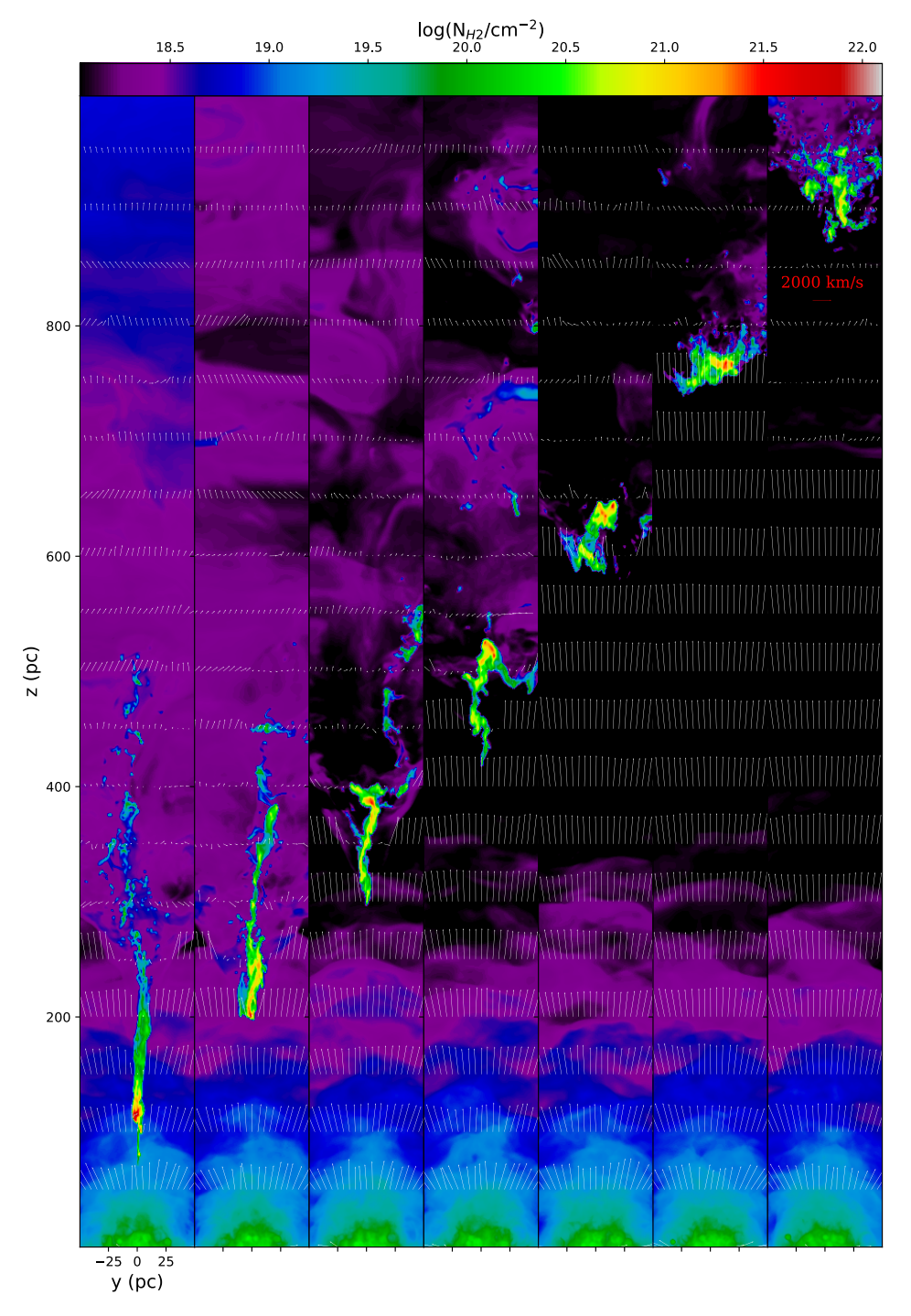


Figure 2. The y-z column density maps of f100n1500v from 1 to 7 Myr, in 1 Myr increments. The white arrows indicate the flow velocity in the x=0 pc slice, with the scale displayed at the upper right.

3.1. X-Ray Emission Projection in a Vertical Magnetic Field

Figures 2 and 3 present the evolution of column density and temperature in the fiducial run. In Figure 2, the high column density $(10^{22} \, \text{cm}^{-2})$ of the MCs can be observed to move away

from the starburst region and eventually flow outside the simulation box. It slows down along the *z*-axis due to the obstruction caused by the clouds. This obstruction leads to the generation of a reverse shock at the contact surface between the shock front and the MCs. At 1 Myr, the starburst-driven

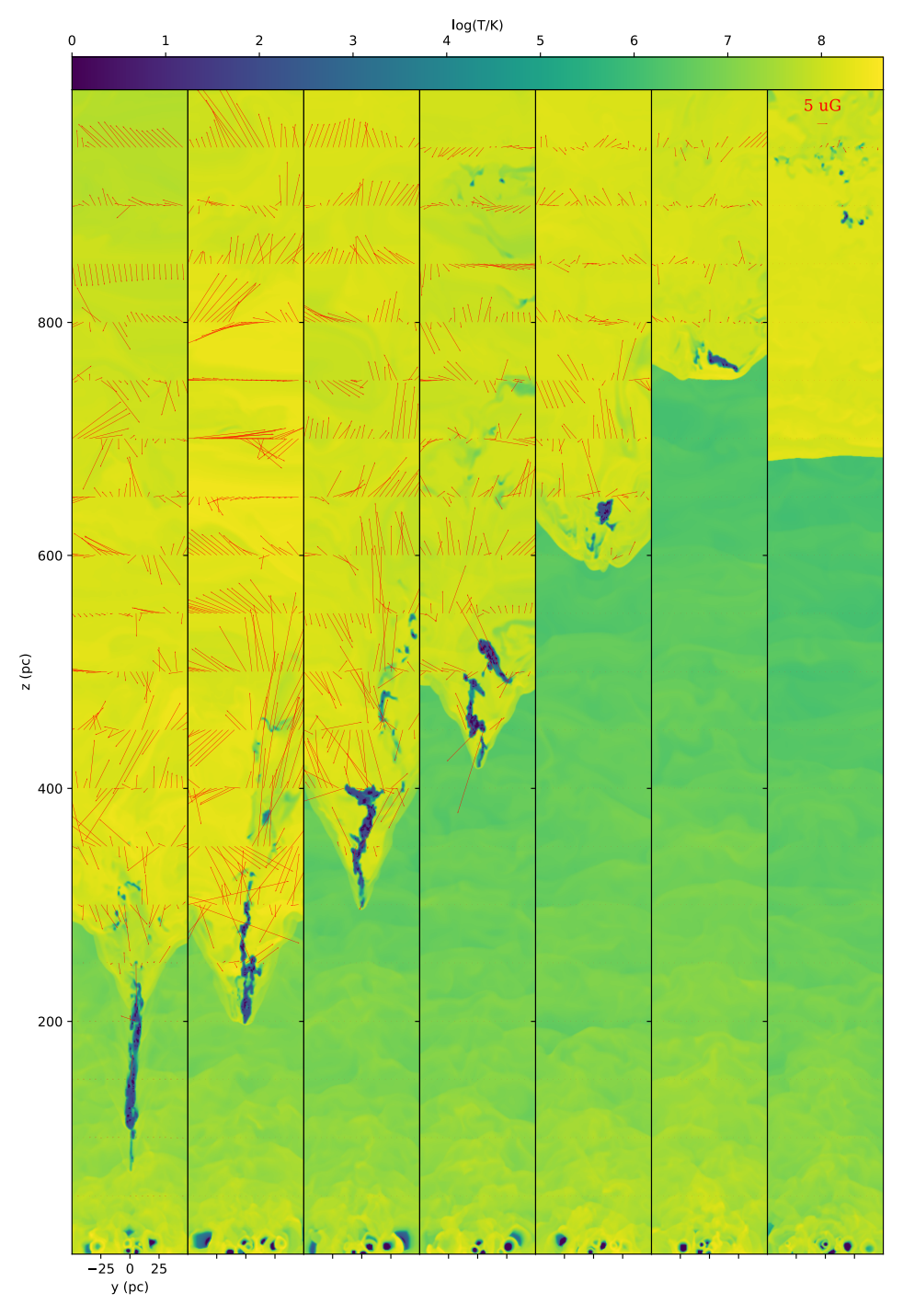


Figure 3. The y-z column temperature slice at x = 0 of f100n1500v from 1 to 7 Myr, in 1 Myr increments. The red arrows show the magnetic field in the x = 0 pc slice, with the scale displayed at the upper right.

wind blows the MCs, elongating the gas that is stripped off the MCs by shock into a filament. At 250 pc, the gas diffuses to obstruct the shock wave, causing the velocity decrease after 250 pc. At 2 and 3 Myr, the shock front is obstructed by the MCs, leading to a gradual compression of the filament which

surrounds the MCs. From 4 to 6 Myr in Figure 2, it can be observed that the filament disappeared, while the envelope gas protects the cloud from wind. The envelope gas continues to expand away from the MCs due to the effects of the shock and reverse shock.

In Figure 3, some low-temperature bubbles can be observed in the starburst region at the bottom, because the SN explosion creates adiabatic expansion. When the shock front has not contacted the MCs, the temperature will decrease with the increase of latitude, because the energy of the starburst outflows takes longer to arrive at the higher latitude. At 1 Myr, the filament below 200 pc has a temperature $T < 10^3$ K, while above 200 pc, the envelope gas with $T > 10^7$ K surrounds the filament. At 2–6 Myr, the envelope gas is characterized by $T > 10^8$ K, surrounding the low-temperature MCs, whereas the ISM temperatures range from $10^6 < T < 10^8$ K. At 7 Myr, the low temperature MCs are almost invisible, but the envelope gas can be seen as diffuse to 700 pc due to the influence of shock. Note that Figure 3 is a slice of x = 0, it is not a projection.

The evolution of X-ray flux for 0.5–2.0 keV is shown in Figure 4. It can be divided into two regions: region A and region B, with our research focusing on the X-ray emission characteristics of gas in region B. In region A, the X-ray fluxes increase when affected by SN explosions, and the X-ray flux will decrease with increasing latitude, until the ISM for latitude above 350 pc is almost unaffected by SN explosions.

At 1 Myr, Figures 2 and 3 show filament of high density and low temperature. But from Figure 4 at 1 Myr, the filament is not clearly visible; the regions of high X-ray flux from the clouds are divided up into two parts: 50–150 pc and 200–500 pc. A comparison between Figures 2 and 4 reveals that the section from 200 to 500 pc corresponds to the tail region of the filament, but the high X-ray flux from 50 to 150 pc is not clear. Since the envelope gas is driven over 200 pc under the influence of shock, the MCs with high density and low temperature between 50–150 pc are not the focus of this study, as this part of gas is not clearly visible in X-rays.

At 2–4 Myr, the MCs are driven to a higher latitude by shock, and the X-ray flux of the high-density and low-temperature MCs is in the range of $10^{-8} \lesssim L_X \lesssim 10^{-6} \, \mathrm{erg \, s^{-1} \, cm^{-2}}$, its X-ray flux is lower than the gas away from the MCs (it is visible at 700 pc of 2 Myr and 650–750 pc of 4 Myr). At 5–7 Myr, the X-ray flux of the MCs is in the range of $10^{-7} \lesssim L_X \lesssim 10^{-5.5} \, \mathrm{erg \, s^{-1} \, cm^{-2}}$.

Figure 5 illustrates a slice taken at 6 Myr. Due to a portion of the shock's velocity changing into an x–y plane, the velocity vector can be seen in the fourth row of Figure 5. The first row shows that the magnitude of velocity, and the velocity within the MC region is over an order of magnitude lower than that of the ISM, indicating the kinetic energy loss is transformed into other energy. At the bottom of the simulation box, SN birth rate of $10 \, \mathrm{kyr}^{-1}$ continuously injects kinetic energy into the box. The kinetic energy partially converts into thermal and magnetic energies, which explains the observed localized enhancement of the magnetic field.

As shown in the third row of Figure 5, the temperature of the envelope gas in region B is an order of magnitude higher than the ISM, indicating that some kinetic energy is converted

into thermal energy, resulting in thermal radiation (this discussion will be further elaborated on in Section 4.3). Additionally, there is some kinetic energy influence on magnetic field enhancement, as shown in the second row of Figure 5, which demonstrates that the magnetic field in region B is 2–5 times greater than that of the initial magnetic field $10 \,\mu\text{B}$, with even more significant increases within the MCs.

This study emphasizes thermal radiation from gas with temperatures exceeding 10⁴ K. In the regions of interaction between an SN remnant (SNR) and clouds, heating mechanisms including photoionization and collisional heating are present (Collins et al. 2005). Additionally, the turbulence at the shock-cloud interface prevents the high-temperature gas from cooling (Li et al. 2020). The magnetic fields in the simulation serve to confine the gas, thereby maintaining its high temperature. As the envelope gas is heated to high temperatures, its density decreases according to the ideal gas law (detailed in Section 4.1). Magnetic confinement sustains the outer envelope gas, which in turn shields the inner MCs, allowing them to maintain higher densities.

From Figure 5, it can be observed that the temperature range of the envelope gas surrounding the MCs, resulting from the interaction of shock, is between 10^7 to 10^9 K, with densities ranging from 10^{-2} to 10^{-1} cm⁻³. The first row of Figure 5 demonstrates the magnitude change of shock velocity within the MC region, where the velocity is significantly lower. The fourth row's velocity vector lines illustrate that the velocity shifts toward the x-y plane and displays turbulence. The second row reveals changes in the magnetic field strength within the MCs due to shock interactions, indicating a notable enhancement of the magnetic field in the MCs. The third row's magnetic field vector lines depict disordered magnetic fields with evidence of magnetic turbulence.

From Figure 5, the envelope gas does not become denser and cooler as it closes the MCs. The conclusion is the MCs, protected by the magnetic field, can maintain a cold and dense state for a prolonged period. In contrast, the envelope gas far from the MCs remains in a state of low density and high temperature (with $n < 10^{-1} \, \mathrm{cm}^{-3}$ and $T > 10^7 \, \mathrm{K}$) due to the effects of the shock. The ISM consistently maintains a state of $n \sim 10^{-3} \, \mathrm{cm}^{-3}$ and $T \sim 10^7 \, \mathrm{K}$, as it is always within the influence of the shock. There is a clear boundary among these three regions.

3.2. X-Ray Emission Projection in Horizontal and No Magnetic Fields

This subsection presents and describes the evolution of X-ray 0.5–2.0 keV flux with horizontal and no magnetic field, illustrated in Figures 6 and 7. In Figure 6, the MCs formed with horizontal magnetic fields exhibit a longer survival time compared to the no magnetic field case. The MCs containing

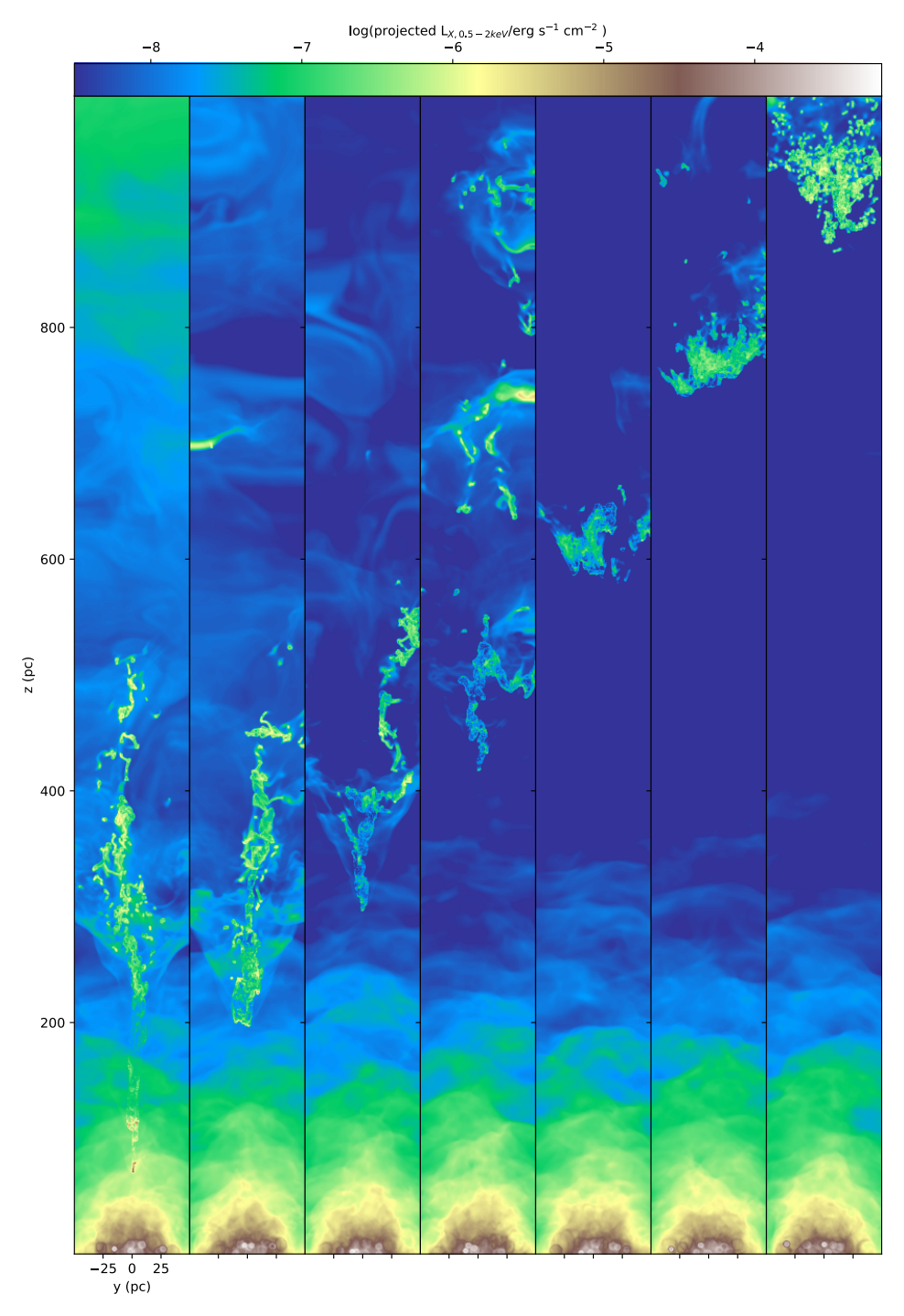


Figure 4. The y-z column X-ray projected emissivity maps of f100n1500v from 1 to 7 Myr, in 1 Myr increments.

 $T < 10^4$ K will not be considered when calculating the X-ray flux. With horizontal magnetic fields, the MCs diffuse faster than the fiducial run due to magnetic turbulence in the x-y plane. Therefore, with the same evolution time, the envelope gas with a horizontal magnetic field will spread wider than the envelope gas with the fiducial run.

In Figures 6 and 7, similar patterns can be observed at 1–2 Myr, including the division of the filament into two high X-ray flux regions at 1 Myr and the shock-driven MCs that moved into low-flux envelope gas at 2 Myr. However, unlike the fiducial run, both Figures 6 and 7 show disruption in their subsequent evolution.

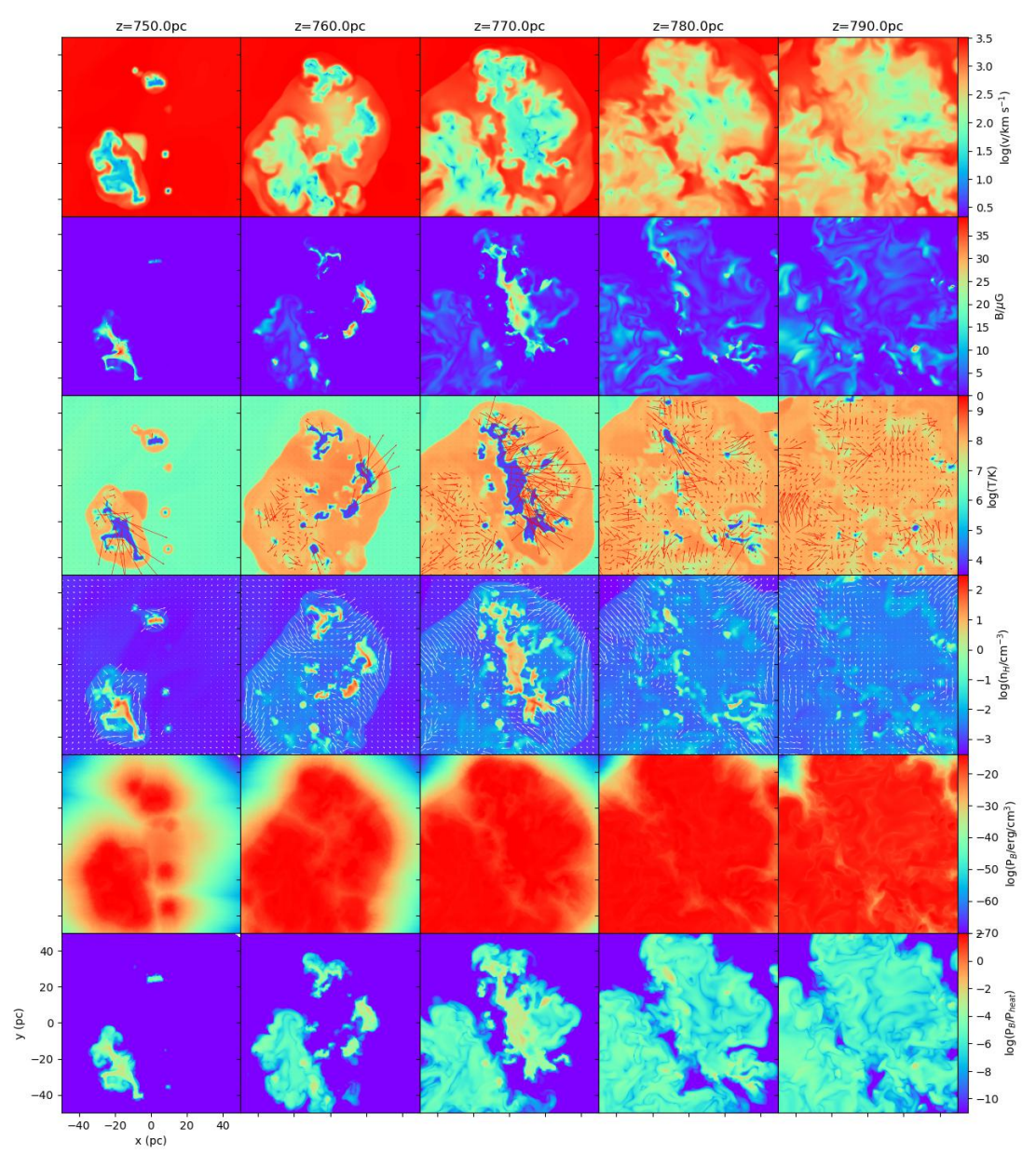


Figure 5. Slice images at 6 Myr under vertical magnetic field, for *z*-axis values of (750.0, 760.0, 770.0, 780.0, 790.0) pc, focusing primarily on the MC region. The first row presents the slice of magnetic induction strength on a logarithmic scale, the second row displays the slice of velocity magnitude, the third row shows the temperature slice, and the fourth row illustrates the slice of number density.

In Figure 6, by 5 Myr, the MCs have fragmented into multiple parts (600–700 pc and z > 800 pc), with a mixture of envelope gas and ISM filling the x-y plane, exhibiting a flux of $L_X \sim 10^{-8} \, \mathrm{erg \, s^{-1} \, cm^{-2}}$. By 6 Myr, the MCs have completely diffused. Similarly, region B in Figure 7 shows a mottled high X-ray flux at 6 Myr. At 8 Myr, the MCs have completely diffused as high X-ray flux ionized gas. Due to the earlier disruption of the clouds, the MCs do not reach latitude comparable to the fiducial run or the horizontal magnetic field.

It is known from Zhang & Li (2024) that in the no magnetic field case, the gas diffuses after a theoretically estimated cloud disruption timescale of $2t_{\rm cc}$. This is also evident in Figure 7. In Figure 7, the MCs without magnetic protection exhibit high flux with $L_X > 10^{-6}\,{\rm erg\,s^{-1}\,cm^{-2}}$, indicating that without a magnetic field, the envelope gas rapidly diffuses across the entire x-y plane. As the evolutionary time increases, the X-ray flux in the envelope gas rises, indicating that the envelope gas completely diffuses and mixes with the ISM.

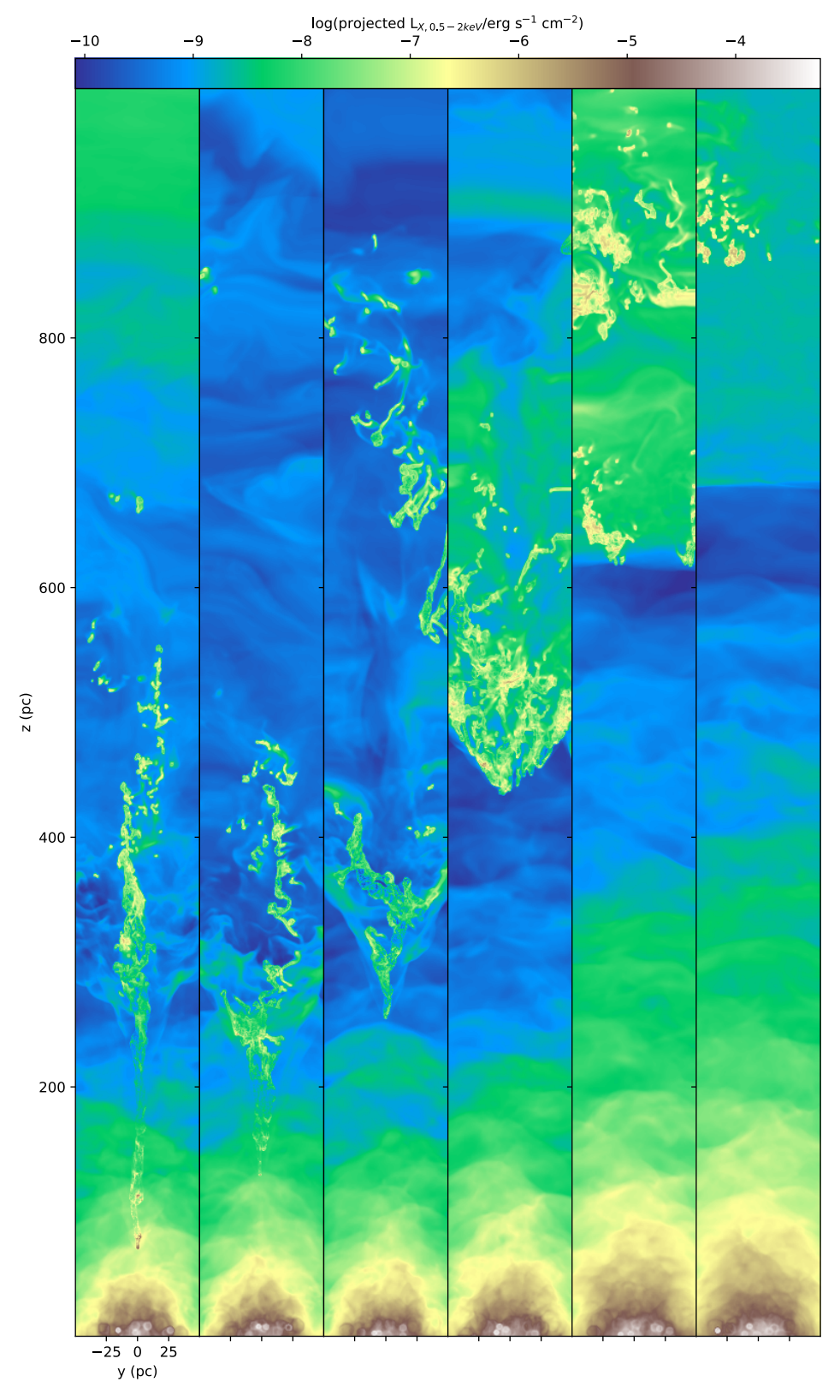


Figure 6. The y-z column X-ray projected emissivity maps of f100n1500h from 1 to 6 Myr, in 1 Myr increments.

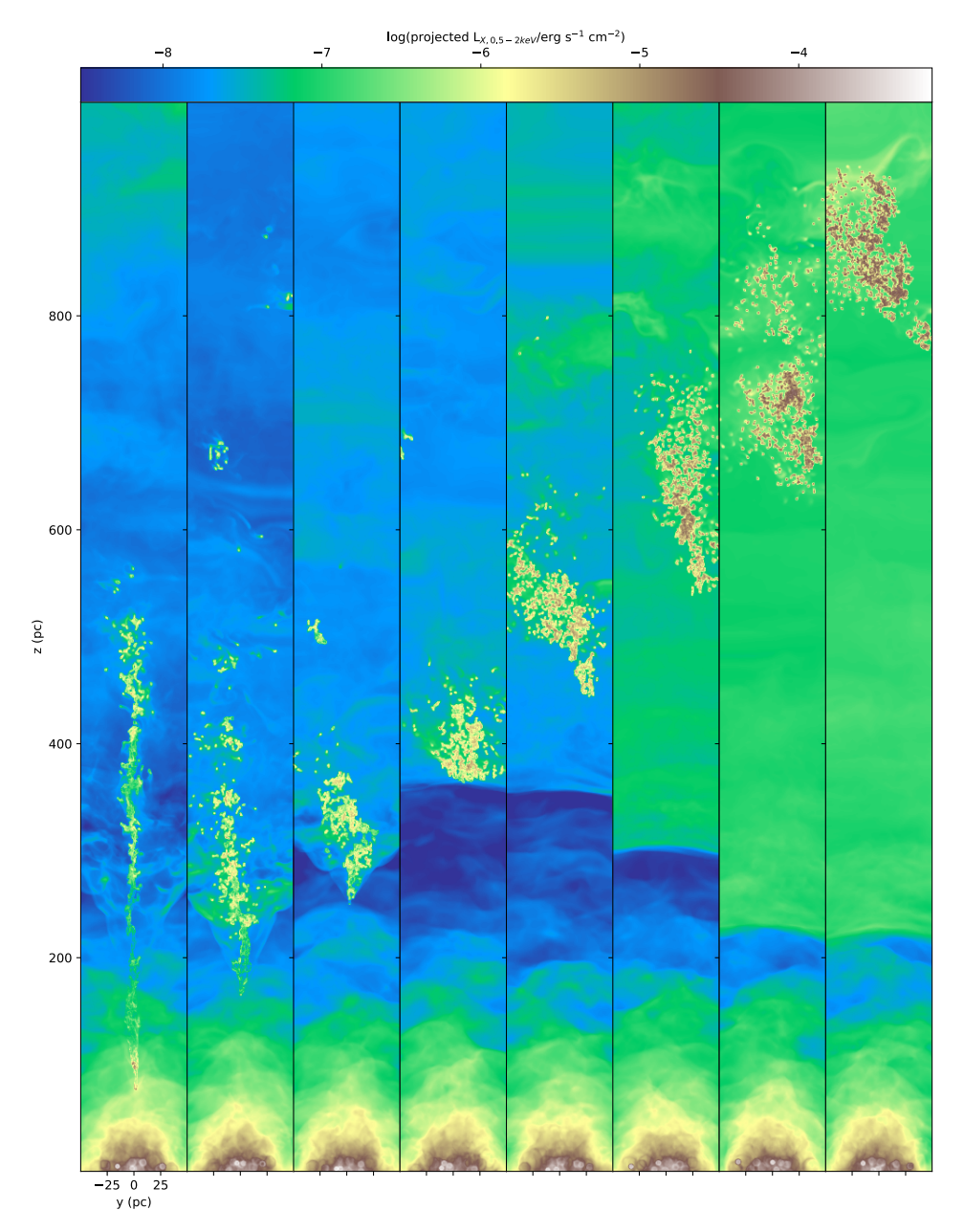


Figure 7. The y-z column X-ray projected emissivity maps of f100n1500n from 1 to 8 Myr, in 1 Myr increments.

4. Discussion

In the previous sections, we presented the results of 3D MHD simulations that utilize the starburst model to study the evolution of the MCs. The simulations were performed with three different magnetic field orientations: vertical, horizontal, and no magnetic field. The X-ray morphology exhibited by these three different magnetic field configurations shows a tight relation between X-ray emission and HVMCs. In this section, we will discuss the results of these simulations and their implications for our comprehension of multi-wavelength structures in the GC.

4.1. X-Ray Evolution of HVMC

Figure 4 shows that the high X-ray flux $(L_X > 10^{-7} \, \mathrm{erg \, s^{-1} \, cm^{-2}})$ is mainly concentrated in the bottom part of the SN birth and the envelope gas. The single SN event can release $10^{51} \, \mathrm{erg}$ energy, and the subsequent SN explosions will continuously heat the bottom region, ionizing the gas and forming an X-ray spectrum. The high X-ray emissivity surrounding the HVMCs arises from the high-temperature envelope gas surrounding the MCs, as shown in Figure 5, where the temperature of the envelope gas is even higher than the ISM. The shock wave strips MCs to form low-density and

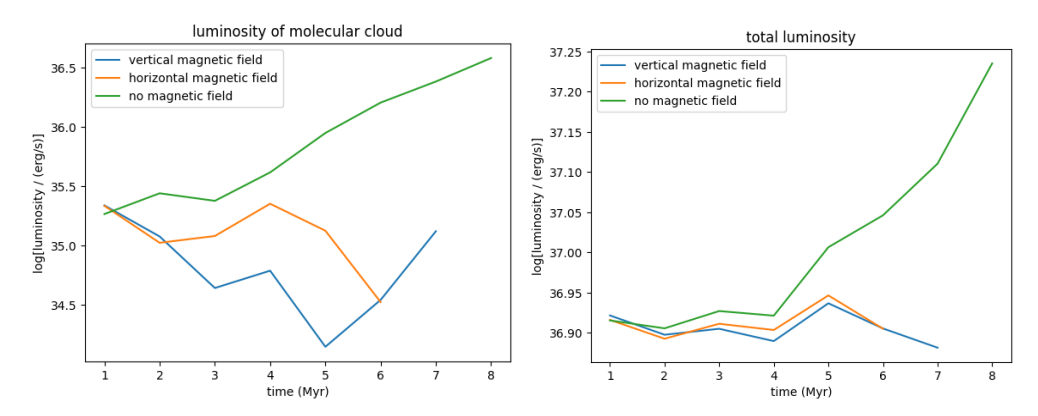


Figure 8. Left: Luminosity evolution curves of MC components. Right: Luminosity evolution curves of gas in the simulation box.

high-temperature envelope gas, which will diffuse gradually in a larger region. Therefore, the envelope gas satisfies the conditions discussed in Equation (3).

Figure 6 shows the X-ray flux with horizontal magnetic field. It is evident that after 3 Myr, the interaction between the horizontal magnetic field and shock leads to the formation of numerous small MC cores. The envelope gas exists between these MC cores, and the high X-ray emissivity is produced by the envelope gas. Consequently, the number of MC cores associated with high X-ray regions is greater than that in Figure 4. This is the same as the findings of Zhang & Li (2024), which suggest the MCs in horizontal magnetic fields are stripped more quickly. Figure 7 shows the results of the no magnetic field run, in which the MCs rapidly disrupt into smaller cores and diffuse envelope gas due to the lack of magnetic protection.

In the cases of vertical, horizontal, and no magnetic fields at 1 Myr, a high X-ray flux region divided into two parts can be observed (see Section 3.1), because the MCs have not been heated when they contact the shock front, while the heated gas is blown away to positions above 200 pc. In Figure 3, it can be seen that at 1 Myr, there is no high-temperature envelope gas surrounding the MCs below 200 pc, with envelope gas only appearing in the region above 200 pc. Additionally, in Figure 2 at 1 Myr, the shock velocity at 250 pc is reduced by the gas with column density $\sim 10^{18.5}$ cm⁻². It can be inferred that the envelope gas below 200 pc diffuses rapidly under the influence of shock.

In Figure 2, after 2 Myr, the distance between MCs and 250 pc is decreasing, indicating that the MCs is gradually moving to higher latitudes under the shock-driven mechanism. After 3 Myr, the envelope gas can be well distinguished from the ISM. Moreover, Figure 4 shows that the X-ray flux of the envelope gas, $\sim 10^{-8} \, \mathrm{erg \, s^{-1} \, cm^{-2}}$, is higher than that of the ISM. The MCs and envelope gas begin to form a compressed clump of HVCs at 5 Myr.

The left panel of Figure 8 shows the temporal evolution of the total luminosity of the gas in region B, while the right

panel shows the temporal evolution of the total luminosity of the entire simulation box. From the left panel, it can be observed that 1–5 Myr in the fiducial run, the total luminosity decreases. This is attributed to the outflow boundary conditions, which causes the envelope gas to leave the simulation box, thereby reducing the luminosity. At 6–7 Myr, the envelope gas is dispersed in a larger region due to the action of shocks, resulting in an increase in luminosity.

In the horizontal magnetic field run, at 1-2 Myr, a portion of the envelope gas exits the simulation box, leading to a decrease in luminosity. At 2-4 Myr, the horizontal magnetic field causes the envelope gas to be widely distributed in the x-y plane. The wide distribution of the envelope gas in the x-y plane increases its contact area with shocks, thereby making the envelope gas more susceptible to shock heating. This process leads to an increase in luminosity. At 4-6 Myr, the luminosity decreases as fragmented MCs are expelled from the simulation box. In contrast, in the no-magnetic field run, the MCs disperse due to lack of magnetic protection after exceeding $t_{\rm cc}$. The fragmented gas mixes with the ISM, but its slightly higher density compared to the ISM causes the luminosity of this portion of gas to increase persistently.

From the right panel, it can be observed that in the presence of a magnetic field, the total luminosity remains relatively stable at 1–4 Myr. At 4–5 Myr, the action of shocks causes the envelope gas to be more widely distributed, leading to a slight increase in luminosity. Subsequently, from 5 to 6 Myr (or up to 7 Myr), the luminosity decreases due to the outflow boundary conditions, which causes the envelope gas to flow away from the simulation box. In contrast, in the absence of a magnetic field, the MCs gradually mix with the ISM, resulting in a continuous increase in luminosity.

The left panel of Figure 9 shows the temporal evolution of the magnetic energy, the kinetic energy and the internal energy for gas in region B, while the right panel presents the corresponding trends for the entire simulation box.

From the upper left panel, we observe that during 1–2 Myr, the magnetic energy in the fiducial run increases due to energy

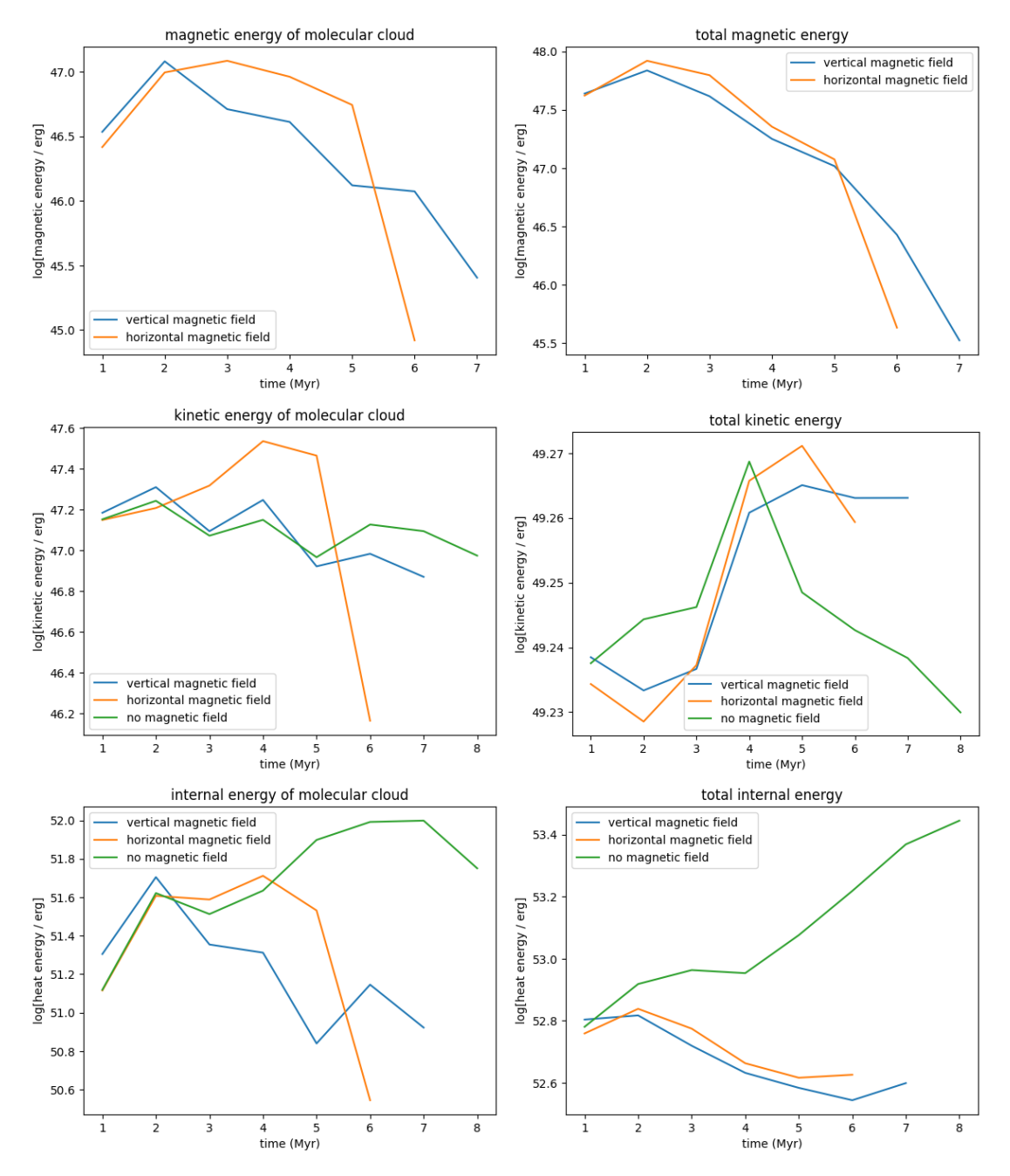


Figure 9. Left: Energy evolution curves of the MC components. From top to bottom, the figure shows the evolution curves of magnetic energy, kinetic energy, and internal energy. Right: Energy evolution curves of gas in the simulation box. From top to bottom, the figure shows the evolution curves of magnetic energy, kinetic energy, and internal energy.

conversion. Subsequently, the magnetic field is expelled from the simulation box by shock interactions. In contrast, horizontal magnetic fields exhibit a similar energy conversion during 1–2 Myr, but their magnetic energy remains relatively stable during 2–5 Myr due to weaker shock-driven expulsion. By 6 Myr, the MC nearly disintegrates and leaves from the simulation box, leading to a sharp decline of magnetic energy. The upper right panel further confirms that the total magnetic

energy initially increases during 1–2 Myr but decreases afterward due to shock effects and gas expulsion from the simulation box.

The middle left panel shows that the kinetic energy in region B exhibits distinct behaviors under different magnetic configurations. In the fiducial run and no-magnetic field run, kinetic energy remains relatively stable. In the fiducial run, this stability arises from the dense configuration of gas in region B,

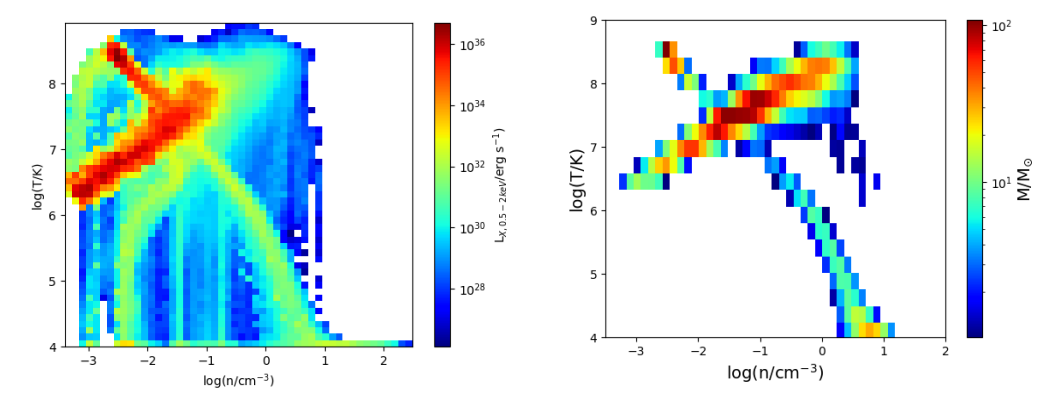


Figure 10. The density-temperature map for f100n1500v at 7 Myr. Left: Temperature–density plot of X-ray luminosity weights temperature–density plot of mass weights. Right: Temperature–density plot of velocity weights.

which suppresses velocity dispersion. In the no-magnetic field run, rapid gas stripping and heating remove heated gas from region B, resulting in stable kinetic energy. For horizontal magnetic fields, the kinetic energy increases until 4 Myr due to cloud tearing and acceleration, after which it declines as the torn cloud exits the simulation box. The middle right panel reveals that the total kinetic energy increases in a magnetized run. However, after 5 Myr, the fiducial run stabilizes, while horizontal magnetic fields show a decline due to gas outflow. In the no-magnetic field run, MC disintegration after 4 Myr (as discussed in Section 2.2) leads to mixing with the ISM and shock heating, resulting in a decline in kinetic energy.

The lower left panel shows that the internal energy in region B increases during 1-2 Myr due to shock heating. In the fiducial run, the internal energy decreases from 2 to 5 Myr as the envelope gas is contaminated by SN jets, reducing the weighting of Q_2 . At 5 and 6 Myr, envelope gas diffuses widely across the x-y plane. As a result of heating, the widely distributed envelope gas causes an increase in the internal energy that subsequently decreases due to the outflow of the envelope gas. For horizontal magnetic fields, the internal energy remains stable from 2 to 5 Myr due to the constant gas temperature. This stability is maintained until the envelope gas flows away from the simulation box, after which the internal energy decreases. In the no-magnetic field run, continuous shock heating leads to a gradual increase in internal energy. The lower right panel confirms that the total internal energy in the magnetized run remains relatively stable, while in the nomagnetic field run, the internal energy increases steadily due to mixing with the ISM and shock heating.

4.2. Phase Diagram of Gas

To understand the gas distribution of the fiducial run, the temperature—density phase diagrams are shown in Figure 10, in which the weighted soft X-ray flux and gas mass are represented in the left and right panels, respectively. This figure contains the component without MCs and the

component of MCs, showing the regions overlapping where temperature and density exhibit direct and inverse proportionality.

The left panel shows two regions of high emissivity $(L_X \gtrsim 10^{35}\,\mathrm{erg\,s^{-1}})$ overlapping, with a density range of $10^{-3} \lesssim \rho \lesssim 10^{-1}\,\mathrm{cm^{-3}}$, and the temperature ranges are: 1. $10^{6.5} \lesssim T \lesssim 10^8\,\mathrm{K}$; 2. $10^7 \lesssim T \lesssim 10^{8.5}\,\mathrm{K}$. In Figure 4, the X-ray flux of the envelope gas is larger than $10^{-6}\,\mathrm{erg\,s^{-1}\,cm^{-2}}$. Although the MCs show low temperatures in Figure 3, the high X-ray flux arises from the envelope gas, which has a temperature $T > 10^7\,\mathrm{K}$, consistent with the earlier discussion.

The left panel of Figure 10 suggests a relationship between high-luminosity gas and multiple processes. To investigate this relationship further, we present the phase diagrams of the component without MCs and the component with MCs separately in the upper left and right panels of Figure 11 respectively.

The upper right panel of Figure 11 shows that only MC components, the remaining gas, exhibit an inverse relationship between temperature and density. In Figure 4, the entire simulation box has been swept by the shock front at 1 Myr, indicating that the shock affects the gas throughout the box in the form of hot wind. At 7 Myr, the MC component can be divided into a high-density, low-temperature part and a high-temperature, low-density part in the envelope gas. The X-ray flux of the high density, low temperature MC gas is negligible, so it will not be discussed further. In contrast, the MC component gas in the envelope gas follows the ideal gas equation

$$P = \rho kT,\tag{4}$$

$$T\rho = \text{constant}.$$
 (5)

In the upper right panel of Figure 11, the black solid lines represent the relationships derived from the isobaric process by both the fixing temperature $T=10^8\,\mathrm{K}$ and density $\rho=10^{-2.1}\,\mathrm{cm}^{-3}$. The line lies within the colored regions of

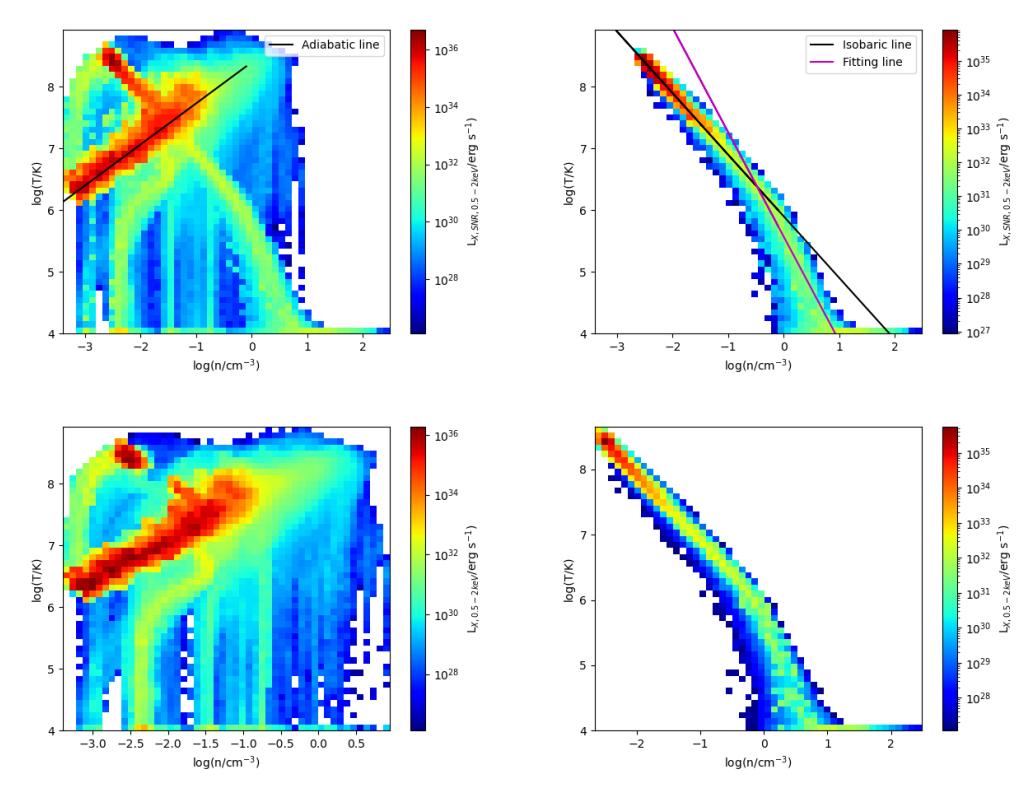


Figure 11. Left: Temperature—density phase diagrams dominated by gas affected by SNe explosions. The upper panel shows the phase diagram using tracer Q_1 , and the lower panel shows the phase diagram for gas in the range of 0–800 pc. Right: Temperature—density phase diagrams dominated by gas with MCs components. The upper panel shows the phase diagram using tracer Q_2 and the lower panel shows the phase diagram for gas in the range of 800–1000 pc.

the phase diagram. This indicates that the high X-ray luminosity gas in this region closely follows the isobaric process.

In the upper right panel of Figure 11, the magenta solid line represents a fitting curve derived under isothermal conditions ($T = 10^6 \,\mathrm{K}$, $\rho = 1 \,\mathrm{cm}^{-3}$). Within the density range of $\rho \in [10^{-3.5}, 10^2] \,\mathrm{cm}^{-3}$, the fitting equation can be expressed as

$$T\rho^{1.695} = 10^{5.57}. (6)$$

The slope of the logarithmic form of Equation (6) exhibits a discrepancy compared to that of Equation (5). This discrepancy arises primarily because the gas in this region is non-thermal-equilibrium material stripped from the surface of MCs, where temperature decreases with proximity to the MC. These gas components reside at the interface between MCs and envelope gas, experiencing compression from the surrounding envelope. Consequently, the density variation spans approximately one order of magnitude.

The upper left panel of Figure 11 shows the phase diagram after masking the MC component. This diagram reveals the coexistence of both inverse and direct relationships between temperature and density. This suggests that the shock influences the entire simulation box. Coupled with previous discussions on the SN shock sweeping across the box, this diagram can be interpreted as representing the temperature—

density relationship in the component without MCs. The density range of the high luminosity area in Figure 11 is between 10^{-3} and 10^{-1} cm⁻³, while the temperature distribution shows two distinct high luminosity regions: 1. $10^{6.5}$ – $10^{7.5}$ K; 2. 10^{7} – $10^{8.5}$ K. Consequently, the high luminosity gas with temperature range of 10^{7} – $10^{8.5}$ K in the component without MCs approximates Equation (5), while other parts follow an adiabatic process (characterized by $\gamma > 1$)

$$\frac{P}{\rho^{\gamma}} = \text{constant}.$$
 (7)

From Equations (4) to (7), we can derive

$$T\rho^{1-\gamma} = \text{constant}.$$
 (8)

To simplify calculations, we take $\gamma=5/3$ for monatomic gases, where P is pressure, ρ is gas density, and T is gas temperature. Thus, the high luminosity gas that shows a direct relationship between temperature and density approximates an adiabatic distribution.

In the upper left panel of Figure 11, the black solid lines represent relationships derived from the adiabatic gas law; fixing both temperature $T=10^7\,\mathrm{K}$ and density $\rho=10^{-2.1}\,\mathrm{cm}^{-3}$, the line lies within the colored regions of the

phase diagram, indicating this gas approximately follows Equation (8).

For the gas near the SN explosion (below 100 pc in latitude), the adiabatic expansion equation (Equation (8)) draws lines that overlap to some extent with the high X-ray luminosity region in the upper left panel of Figure 11, indicating that this gas can be explained by the adiabatic expansion process. Conversely, the gas outside this region aligns with the isobaric process (Equation (5)). This is evidenced by in the upper right panel of Figure 11, which exhibits an inverse relationship between temperature and density. This suggests that the gas in this region can be explained by the isobaric process.

The bottom left of Figure 11 is the phase diagram below 800 pc; the bottom right of Figure 11 is the phase diagram above 800 pc. We can see in the bottom left of Figure 11 that there is a high X-ray emissivity gas at temperature $\sim 10^{8.5}$ K and density $\sim 10^{-2.5}$ cm⁻³. The source of this high X-ray emissivity gas is formed by the reverse shock driving the envelope gas to diffuse below 800 pc.

4.3. Diffusive HVC Gas

In the simulations, it is challenging to accelerate the MCs to 200 km s⁻¹ and kpc scales without disruption (Schneider & Robertson 2017; Cashman et al. 2021). This study explores the survival of the MCs under the influence of starburst-driven winds in different magnetic field environments, including a case with no magnetic field. The conclusion is that a vertical magnetic field can protect clouds to maintain a size of approximately 50 pc as they flow outside the simulation box. Although a horizontal magnetic field also increases the survival time of the MCs compared to the no-magnetic field scenario, the clouds begin to diffuse after 5 Myr.

A noteworthy aspect is that magnetic fields can extend the survival time of MCs. Aluzas et al. (2014) mentioned that clouds can "slingshot" against each other, allowing them to propagate relative to each other in the direction perpendicular to the shock. In the presence of a vertical magnetic field, the gas pressure formed by the shock hinders the escape of gas within the MC region (as seen in the fourth row of Figure 5, where gas accumulates to form a high-density ring structure). The gas confined within the MCs influences the magnetic field, which accounts for the chaotic magnetic field lines seen in the third row of Figure 5. Additionally, the shock waves compress and amplify the magnetic field within the MCs, and the highdensity MCs move along the z-axis, resulting in an approximately ring-like magnetic field in the x-y plane (visible in the fourth row, third column of Figure 5). At this point, the gas within the MCs forms a magnetic confinement state. Schneider & Robertson (2017) indicated that different temperature gases distribute momentum similarly, supporting the idea that the ring structure impedes gas outflow, reinforcing the notion of magnetic confinement.

In Aluzas et al. (2014), it was mentioned that clouds along the same magnetic field line can merge, while clouds on different magnetic field lines that are compressed together may lead to "rebound" interactions. In a vertical magnetic field, the magnetic field lines of clouds are aligned along the z-axis and are parallel to each other, facilitating merging between low-latitude and high-latitude gases. In a horizontal magnetic field, the close packing of clouds results in rebound interactions, forming multiple small MC core regions. The presence of a magnetic field provides a protective magnetic confinement for the clouds, making them less likely to disperse. However, under external pressure, horizontal magnetic fields can accelerate the disruption of clouds.

The slices from Figure 5 help to elucidate the detailed relationships between the MCs, the envelope gas, and the ISM at a 100 pc scale. From Figure 5, it is clear that with magnetic protection, there is a distinct division based on temperature and density between the MCs, the envelope gas, and the ISM at 6 Myr. Intuitively, a lower temperature is expected at the region closer to the MCs, but it is perplexing to observe a significant jump in temperature (or density) directly between the MCs and the envelope gas. With magnetic confinement, only a small portion of the MC gas is stripped, causing it to diffuse outward and form the envelope gas.

The density slice in Figure 5 shows that the velocity within the envelope gas is low, with significant outward diffusion velocity only at the interface between the envelope gas and ISM. This indicates that the shock wave drives the diffusion of envelope gas, resulting in a high-velocity, high-density ring structure near the interface of the envelope gas and the ISM, while the density and temperature within this ring remain stable relative to the ISM. Due to the shock and reverse shock effects on the MC region, the velocity variations of the gas within the MCs are dramatic compared to the ISM, leading to velocity vectors that can be interpreted as turbulence. This allows for an extended cooling time for the high-temperature gas in the envelope (Li et al. 2020), which is the reason why the temperature of the envelope gas is higher than that of the ambient gas.

The enhanced magnetic field in the MCs is related to electromagnetic induction amplification; the high-density gas in the MCs result in a high magnetic field in that region. In contrast, the magnetic field enhancement in the envelope gas is related to the effects such as Kelvin–Helmholtz instability and Richtmyer–Meshkov instability, which converts kinetic energy into magnetic energy, explaining the presence of magnetic turbulence in the envelope gas. Whether due to magnetic pressure or instability, the velocity of the gas will affect the orientation of the magnetic field lines.

The emission spectra of continuous spectrum X-rays, $H\alpha$, O VII, O VIII and Fe L-shell are presented in Figure 12, showcasing the emission at 6 Myr with the fiducial run. The first row of Figure 12 displays the X-ray emission continuum

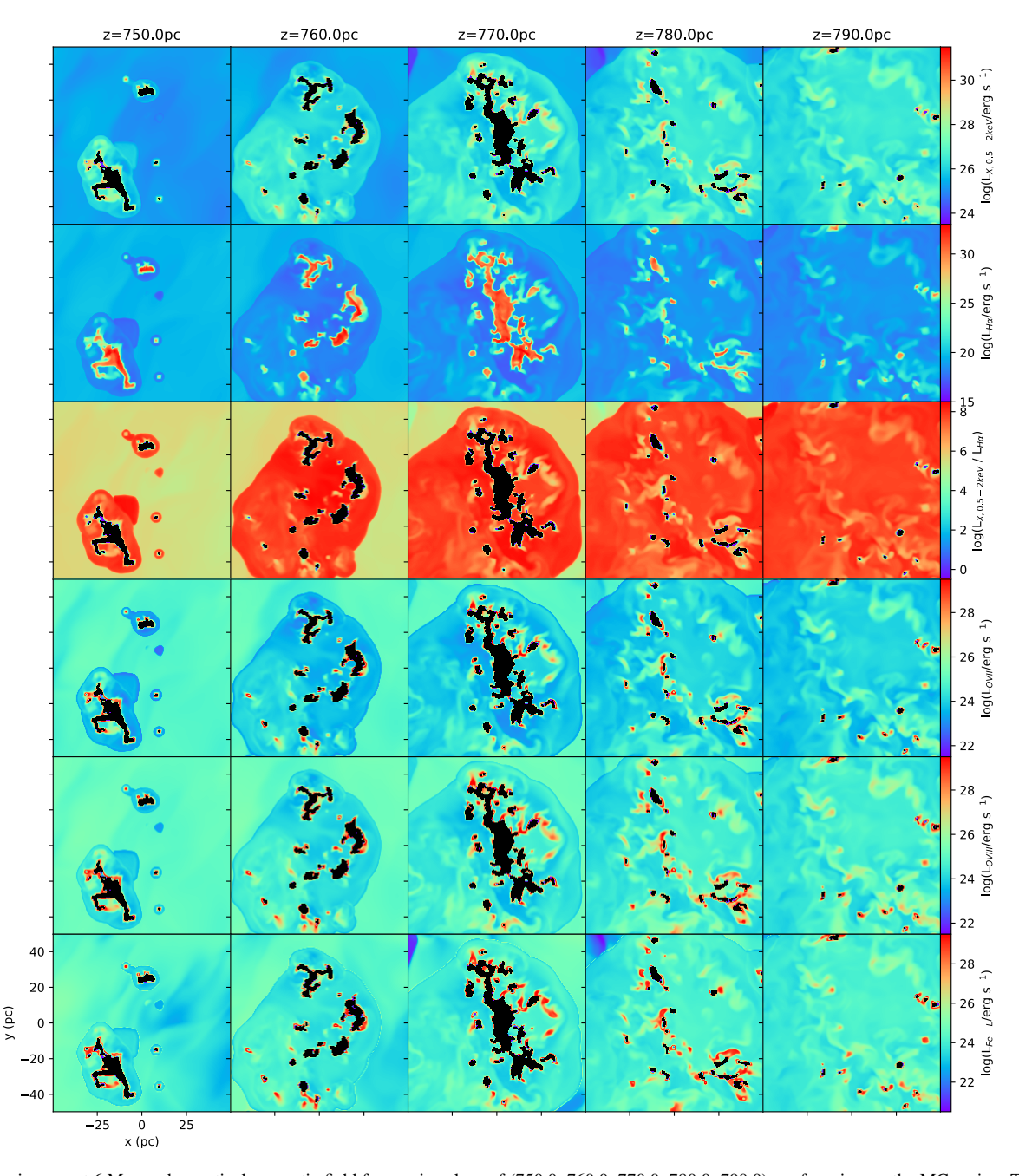


Figure 12. Slice images at 6 Myr under vertical magnetic field for z-axis values of (750.0, 760.0, 770.0, 780.0, 790.0) pc, focusing on the MC region. The first row represents soft X-ray emission, the second row shows $H\alpha$ emission, the third row shows the ratio of soft X-ray emission and $H\alpha$ emission, the fourth row displays O VII line emission, the fifth row presents O VIII line emission, and the sixth row illustrates Fe L-shell line emission.

spectrum slice, and the envelope gas was observed to have the highest X-ray flux.

The second row of Figure 12 displays the $H\alpha$ emission slice, indicating that areas of high density correspond to higher $H\alpha$ emissivity. The recombination rate coefficient used for calculating the $H\alpha$ line radiation emissivity follows the description in Draine (2010), expressed in Equation (9). The

calculation formula for the ${\rm H}\alpha$ line emission emissivity is given by Equation (10),

$$\alpha_{\rm eff, H\alpha} \approx 1.17 \times 10^{-13} T_4^{-0.942 - 0.031 \ln T_4} \, {\rm cm}^3 \, {\rm s}^{-1},$$
 (9)

$$L_{\text{H}\alpha} = \alpha_{\text{eff},\text{H}\alpha} \quad n_e n_p h v_{\text{H}\alpha} \text{ erg cm}^{-3} \text{ s}^{-1}, \tag{10}$$

where h is the Planck constant, n_e the electron number density, n_p the proton number density, $v_{\text{H}\alpha}$ the frequency of the H α line, and $T_4 = T/10,000$.

The third row of Figure 12 shows the ratio of soft X-ray emission and $H\alpha$ emission. It can be seen from the figure that the X-ray emissivity is greater than $H\alpha$ emission in envelope gas and ISM, but the gas approaching MCs has $H\alpha$ emission greater than the X-ray emissivity.

The fourth, fifth, and sixth rows of Figure 12 present the X-ray emission emissivity slices for O VII, O VIII, and Fe L-shell lines, respectively, with the spectral bands referenced from Pan et al. (2024). These slices exhibit similar overall patterns, but O VII and O VIII lines show higher emission emissivities in the ISM compared to Fe L-shell. This discrepancy could be attributed to the difference in temperature of the gas, and the emissivity of a particular element will be greatest only at the temperatures optimal for emission. The temperatures optimal for emission of O VII, O VIII, and Fe L-shell are given in Pan et al. (2024), which are $\sim 2 \times 10^6$ K, $\sim 3 \times 10^6$ K, and $\sim 7 \times 10^6$ K, respectively. Therefore, we can see that gas with a temperature $\sim 10^8$ K has a lower emissivity at O VII, O VIII and Fe L-shell, while the gas with a $10^6 \lesssim T \lesssim 10^7$ K has a higher emissivity.

In the context of interactions between the MCs, the envelope gas and the ISM, the shock and MC interactions can lead to Richtmyer-Meshkov instability due to velocity differences across gas interfaces, as well as Kelvin–Helmholtz instability caused by those same differences. Additionally, density differences across gas interfaces can give rise to Rayleigh–Taylor instability. These instabilities significantly affect the distribution of temperature, density, velocity, and magnetic fields within the fluid, and this topic will be a focus of future research.

4.4. The Relationship between HVMC and Feedback

In the simulations, the X-ray flux from the low-temperature MCs is negligible compared to the radiation from the surrounding envelope gas. However, for the MCs at temperatures $T\lesssim 10^4$ K, the H α emission becomes more important. Figure 12 also shows that the H α luminosity of the MCs is $L_{\alpha}\gtrsim 10^{30}\,\mathrm{erg}\,\mathrm{s}^{-1}$, implying a relation between the soft X-ray and H α emission of HVMCs.

In Mineo et al. (2012), soft X-ray luminosity for multiple galaxies was presented. Although the data are not derived from hot gas in the GC, they provide a sufficient reference for the magnitude of soft X-ray luminosity. The study shows that the soft X-ray luminosity ranges from $\log(L_X) \sim 37$ –39. In our simulation, the soft X-ray luminosity is 5.17×10^{37} erg s⁻¹, a similar order of magnitude. Additionally, both Mineo et al. (2012) and Kyritsis et al. (2025) noted that the ratio of L_X to SFR remains constant, with the value provided by Mineo et al. (2012) being $L_X/\text{SFR} \approx 8.3 \times 10^{38}\,\text{erg s}^{-1}\,\text{per}\,M_\odot\,\text{yr}^{-1}$. Given

that our simulation's SFR is $1 M_{\odot} \text{ yr}^{-1}$, we derive $L_X/\text{SFR} \approx 5.2 \times 10^{37} \, \text{erg s}^{-1} \, \text{per} \, M_{\odot} \, \text{yr}^{-1}$, while differing by an order of magnitude. Because the other sources, such as nuclear winds, AGN winds and CGM hot gas, are neglected in the simulation, the value is lower than what is provided by the observations.

In Section 3, the role of magnetic fields in maintaining the MCs was highlighted. In the fiducial run, from 1 to 3 Myr, shock-driven MCs form filaments due to magnetic influences (Zhang & Li 2024). Additionally, Heywood et al. (2019) observed filaments in the radio band and noted a correspondence between radio bubbles and X-ray emissions, suggesting a common origin. This study focuses on the X-ray band of 0.5-2 keV; however, other radiation bands may generate unexpected results in studying the effects of nuclear winds on the MCs. For instance, Ponti et al. (2013) noted that X-ray emission irradiation can release silicon from dust in the form of SiO, thereby enhancing the $K\alpha$ line emission. Consequently, in cold gas exposed to high X-ray fluxes, $K\alpha$ emission may be more readily detectable. Nevertheless, as dust was not incorporated into our simulation, the $K\alpha$ values are likely underestimated; observations could reveal higher values.

The morphological correlation between radio bubbles and X-rays highlighted by Heywood et al. (2019) suggests a common origin and presents a promising avenue for further investigation. Additionally, Ponti et al. (2019) proposed that MCs transport energy to higher latitudes via X-ray chimneys, indicating that small-scale simulation of MCs can effectively bridge connections among MCs, X-ray chimneys, and radio bubble structures.

The study by Walch & Naab (2015) indicates that SNe in low-density environments show enhanced kinetic energy transfer to the surrounding medium and higher momentum injection efficiency, thereby driving stronger outflows. However, observational evidence shows that SNe mainly occur in high-density regions or areas with active star formation. The random SN injection approach might overestimate the strength of the outflows, as the random SN injection within a cylindrical region (radius of 35 pc and height of 10 pc) could cause SN injection in low-density regions, making the outflow stronger than observed.

Our use of the random SN injection approach aims to simplify the simulation while ensuring a uniform distribution of SN explosions within a cylindrical region. This method is reasonable for studying the impact of nuclear winds on large-scale regions. However, it has limitations when it comes to investigating small-scale gas dynamics and energy transfer.

5. Conclusions

To study the formation of the HVMCs at the GC, we suggest a starburst driven model and estimate its X-ray emission. The X-ray flux surrounding HVMCs is usually not

expected because the cold MCs do not have temperatures optimal for emission of soft X-rays. However, our simulation results show that the gas stripped from the MCs can be heated to high temperature and produce soft X-ray emission.

The main findings are summarized as follows:

- 1. The gas stripped from the MCs can produce soft X-ray emission, the gas is high temperature and low density, which is named envelope gas. In Figure 5, a clear boundary exists between the envelope gas and the MCs. In the interaction between the envelope gas and shock wave, the envelope gas protects the MCs from shock wave.
- In Figure 5, the magnetic fields are compressed and amplified in the MCs. The presence of magnetic fields places the clouds in a magnetic confinement state, protecting the clouds from the destruction of the shock wave.
- 3. In Figure 12, the correlation between $H\alpha$ and soft X-ray emission is obvious.
- 4. The simulation results support the transport of energy from small scale to large scale.

Acknowledgments

We acknowledge the cosmology simulation database (CSD) in the National Basic Science Data Center (NBSDC) and its funds the NBSDC-DB-10. We acknowledge the support from the National Key Research and Development Program of China (2022YFA1602930), the National Natural Science Foundation of China (NSFC, grant Nos. 11825303 and 11861131006), the science research grants from the China Manned Space project with No. CMS-CSST 2021-A03, CMS-CSST-2021-A04, the Fundamental Research Funds for the Central Universities of China (2262022-00216) and the start-up funding of Zhejiang University.

Appendix A Spherical Model

For the NSC and the ND, we adopt a spherical distribution following Chatzopoulos et al. (2015). Assuming a constant mass-to-light ratio and including a black hole, the potential is modeled as the gravitational potential (Dehnen 1993)

$$\Psi(r) = \sum_{i=1}^{2} \frac{GM_i}{a_i} \frac{1}{(2 - \gamma_i)} \left(1 - \left(\frac{r}{r + a} \right)^{2 - \gamma_i} \right) + \frac{GM_{\bullet}}{r}.$$
 (A1)

Here, M_{\bullet} is the mass of the black hole. The parameters used in the simulation can be found in Table A1. Given that the

Table A1
This is the Gravitational Parameter Chart

Scale	γ_1	γ_2	a_1	a_2	M_2/M_1
(1)	(2)	(3)	(4)	(5)	(6)
Small Scale	0.51	0.07	99	2376	105.45
Lager Scale	0.71	0.07	147.6	4572	101.6

Note. (1) Model Scale Type. (2) γ_1 index. (3) γ_2 index. (4) Scaling radius of the NSC, in arcsec. (5) Scaling radius of the ND, in arcsec. ,(6) Mass ratio, where $M_1=6.3\times 10^7 M_{\odot}$.

potential and density are known, we can numerically compute the distribution function (DF) using Eddington's formula, defined in terms of positive energy $E=\Psi-\frac{1}{2}\upsilon^2$

$$f(E) = \frac{1}{\sqrt{8}\pi^2} \left[\int_0^E \frac{d\Psi}{\sqrt{E - \Psi}} \frac{d^2\rho}{d\Psi^2} + \frac{1}{\sqrt{E}} \left(\frac{d\rho}{d\Psi} \right)_{\Psi=0} \right]. \tag{A2}$$

This formula is used to calculate the DF f(E), where E is the energy, ρ is the density, and Ψ is the gravitational potential.

The second term in the equation disappears under reasonable assumptions about the behavior of the potential. The double derivative inside the integral can be simplified using the transformation

$$\frac{d^2\rho}{d\Psi^2} = -\left[\left(\frac{d\Psi}{dr} \right)^{-3} \frac{d^2\Psi}{dr^2} \right] \frac{d\rho}{dr} + \left(\frac{d\Psi}{dr} \right)^{-2} \frac{d^2\rho}{dr^2}.$$
 (A3)

The DF remains positive for all energies. To test the accuracy of the DF, we can reconstruct the density using the formula

$$\rho(r) = 4\pi \int_0^{\Psi} dE \ f(E) \sqrt{\Psi - E}. \tag{A4}$$

The DF exhibits the typical shape of models with a shallow cusp (where $\gamma < 3/2$). It decreases as a function of energy both near the black hole and for large energies. Additionally, it reaches a maximum near the binding energy of the stellar potential well (Baes et al. 2005).

Appendix B Cooling Function

The cooling process can significantly influence the evolution of HVMCs, but an accurate tabulated cooling function will spend much more computational resource. Therefore, in the simulations, we adopt a piecewise cooling function (see Figure B1), which can roughly describe the cooling function.

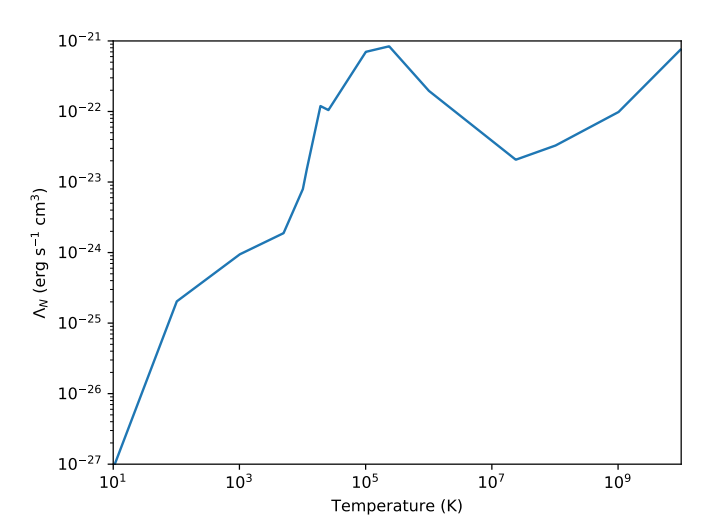


Figure B1. The piecewise cooling curve used in the simulations.

References

Aluzas, R., Pittard, J. M., Falle, S. A. E. G., & Hartquist, T. W. 2014, MNRAS, 444, 971 Ashley, T., Fox, A. J., Jenkins, E. B., et al. 2020, ApJ, 898, 128 Baes, M., Dejonghe, H., & Buyle, P. 2005, A&A, 432, 411 Baganoff, F. K., Maeda, Y., Morris, M., et al. 2003, ApJ, 591, 891 Beck, R., Balogh, A., Bykov, A., Treumann, R. A., & Widrow, L. 2013, Large-Scale Magnetic Fields in the Universe (Berlin: Springer) Bland-Hawthorn, J., Maloney, P. R., Sutherland, R., et al. 2019, ApJ, 886, 45 Bordoloi, R., Fox, A. J., Lockman, F. J., et al. 2017, ApJ, 834, 191 Carretti, E., Crocker, R. M., Staveley-Smith, L., et al. 2013, Natur, 493, 66 Cashman, F. H., Fox, A. J., Savage, B. D., et al. 2021, ApJL, 923, L11 Cerri, S. S., Gaggero, D., Vittino, A., Evoli, C., & Grasso, D. 2017, JCAP, Chatzopoulos, S., Fritz, T. K., Gerhard, O., et al. 2015, MNRAS, 447, 948 Collins, J. A., Shull, J. M., & Giroux, M. L. 2004, ApJ, 605, 216 Collins, J. A., Shull, J. M., & Giroux, M. L. 2005, ApJ, 623, 196 Dehnen, W. 1993, MNRAS, 265, 250 Di Teodoro, E. M., McClure-Griffiths, N. M., Lockman, F. J., & Armillotta, L. 2020, Natur, 584, 364 Di Teodoro, E. M., McClure-Griffiths, N. M., Lockman, F. J., et al. 2018, ApJ,

```
Draine, B. T. 2010, Physics of the Interstellar and Intergalactic Medium, Vol.
   19 (Princeton, NJ: Princeton Univ. Press)
Fabian, A. C. 2012, ARA&A, 50, 455
Ferrière, K. 2009, A&A, 505, 1183
Finkbeiner, D. P. 2004, ApJ, 614, 186
Foster, A., Smith, R. K., Brickhouse, N. S., & Cui, X. 2016, AAS/HEAD
  meeting, 15, 116.18
Fox, A. J., Bordoloi, R., Savage, B. D., et al. 2015, ApJL, 799, L7
Fujita, Y., Ohira, Y., & Yamazaki, R. 2013, ApJL, 775, L20
Guo, F., & Mathews, W. G. 2012, ApJ, 756, 181
Haywood, M., Lehnert, M. D., Di Matteo, P., et al. 2016, A&A, 589, A66
Heckman, T. M., & Best, P. N. 2014, ARA&A, 52, 589
Heckman, T. M., & Thompson, T. A. 2017, in Galactic Winds and the Role
  Played by Massive Stars, Handbook of Supernovae, ed. A. W. Alsabti &
  P. Murdin (Cham: Springer Int. Publishing), 2431
Heywood, I., Camilo, F., Cotton, W. D., et al. 2019, Natur, 573, 235
Kataoka, J., Tahara, M., Totani, T., et al. 2013, ApJ, 779, 57
Klein, R. I., McKee, C. F., & Colella, P. 1994, ApJ, 420, 213
Kroupa, P. 2001, MNRAS, 322, 231
Kyritsis, E., Zezas, A., Haberl, F., et al. 2025, A&A, 694, A128
Lacki, B. C. 2014, MNRAS: Letters, 444, L39
Li, M., Li, Y., Bryan, G. L., Ostriker, E. C., & Quataert, E. 2020, ApJ, 898, 23
Lockman, F. J., Di Teodoro, E. M., & McClure-Griffiths, N. M. 2020, ApJ,
Mannucci, F., Della Valle, M., Panagia, N., et al. 2005, A&A, 433, 807
McClure-Griffiths, N. M., Green, J. A., Hill, A. S., et al. 2013, ApJL, 770, L4
Mignone, A., Bodo, G., Massaglia, S., et al. 2007, ApJS, 170, 228
Mignone, A., Zanni, C., Tzeferacos, P., et al. 2012, ApJS, 198, 7
Mineo, S., Gilfanov, M., & Sunyaev, R. 2012, MNRAS, 426, 1870
Naab, T., & Ostriker, J. P. 2017, ARA&A, 55, 59
Pan, Z., Qu, Z., Bregman, J. N., & Liu, J. 2024, ApJS, 271, 62
Planck Collaboration, Ade, P. A. R., Aghanim, N., et al. 2013, A&A,
  554, A139
Ponti, G., Hofmann, F., Churazov, E., et al. 2019, Natur, 567, 347
Ponti, G., Morris, M. R., Terrier, R., & Goldwurm, A. 2013, Cosmic Rays in
  Star-Forming Environments (Berlin Heidelberg: Springer), 331
Predehl, P., Sunyaev, R. A., Becker, W., et al. 2020, Natur, 588, 227
Sarkar, K. C., Nath, B. B., & Sharma, P. 2015, MNRAS, 453, 3827
Schneider, E. E., & Robertson, B. E. 2017, ApJ, 834, 144
Sofue, Y., & Handa, T. 1984, Natur, 310, 568
Su, M., Slatyer, T. R., & Finkbeiner, D. P. 2010, ApJ, 724, 1044
Walch, S., & Naab, T. 2015, MNRAS, 451, 2757
Zhang, D. 2018, Galax, 6, 114
Zhang, M., & Li, M. 2024, MNRAS, 527, 3418
Zhang, M., Li, Z., & Morris, M. R. 2021, ApJ, 913, 68
Zhang, R., & Guo, F. 2020, ApJ, 894, 117
Zubovas, K., & Nayakshin, S. 2012, MNRAS, 424, 666
```